

Synthesis and characterization of $\text{SrFe}_x\text{Mn}_{1-x}(\text{O},\text{F})_{3-\delta}$ oxide ($\delta = 0, 0.5$) and oxyfluoride perovskite films

*Jiayi Wang, Benjamin M. Lefler, Steven J. May**

Department of Materials Science and Engineering, Drexel University, Philadelphia, Pennsylvania 19104, USA

Keywords: oxyfluorides, *B*-site alloyed perovskite, electronic transport, optical absorption

Abstract

We report the synthesis and characterization of as-grown $\text{SrFe}_x\text{Mn}_{1-x}\text{O}_{2.5}$ epitaxial films, which were also subjected to post-growth oxidation and topotactic fluorination to obtain $\text{SrFe}_x\text{Mn}_{1-x}\text{O}_3$ and $\text{SrFe}_x\text{Mn}_{1-x}\text{O}_{2.5-\delta}\text{F}_\gamma$ films. We show how both the *B*-site cation and anion composition influence the structural, electronic, and optical properties of this family of perovskite materials. The Fe substitution of Mn in $\text{SrMnO}_{2.5}$ gradually expands the *c*-axis parameter, as indicated by X-ray diffraction. With increasing *x*, the F content incorporated under identical fluorination conditions increases, reaching its maximum in $\text{SrFeO}_{2.5-\delta}\text{F}_\gamma$. In the compounds with mixed *B*-site occupation, the Fe 2*p* photoemission peaks are shifted upon fluorination while the Mn 2*p* peaks are not, suggesting inductive effects lead to asymmetric responses in how F alters the Mn and Fe bonds. Electronic transport measurements reveal all compounds are insulators, with the exception of SrFeO_3 , and demonstrate that fluorination increases resistivity for all values of *x*. Optical absorption spectra in the $\text{SrFe}_x\text{Mn}_{1-x}\text{O}_{2.5}$ and $\text{SrFe}_x\text{Mn}_{1-x}\text{O}_3$ films evolve systematically as a function of *x*, consistent with a physical scenario in which optical changes with Fe substitution

arise from a linear combination of Mn and Fe 3d bands within the electronic structure. In contrast, the F incorporation induces non-linear changes to the optical response, suggesting a more complex impact on the electronic structure in materials with concurrent *B*-site and anion site substitution.

Introduction

Controlling the composition and occupation of the anion site is a dominant strategy for tuning the functionality of transition metal perovskites.¹ For example, introducing oxygen vacancies into $ABO_{3-\delta}$ perovskite oxides is an important means to induce and engineer many interesting properties, such as magnetism, electronic and ionic conductivity, and catalytic activity.^{2,3} These oxygen-deficient perovskites crystallize in a large variety of structures depending on the degree of anion deficiency, cation composition, and vacancy ordering.⁴ Among them, oxygen-deficient perovskites with the formula $ABO_{2.5}$ ($\delta = 0.5$) have attracted attention due to the unique arrangements of oxygen vacancies found in these materials, where typically the $ABO_{3-\delta}$ notation is used to indicate materials with disordered (or uncharacterized) vacancy occupations while integer formula such as $A_2B_2O_5$ indicate crystallographic ordering of vacancies. One example is the $A_2B_2O_5$ brownmillerite structure, in which half of the *B* cations are octahedrally coordinated, forming BO_6 corner-sharing layers, and the other half of the *B* cations (*B'*) are tetrahedrally coordinated, forming $B'O_4$ corner-sharing chains within the plane where oxygen vacancies are located.^{5,6} A schematic of the brownmillerite structure is shown in Figure 1a. Compared with the dense ABO_3 perovskite pseudocubic lattice, the ordering of oxygen vacancies in $A_2(BB')O_5$ brownmillerites has been suggested as a way of enhancing the mobility of oxygen ions, which makes this materials family a promising electrolyte candidate for solid oxide fuel cells; $Ba_2In_2O_5$, $Sr_2Co_2O_5$, and $Sr_2Fe_2O_5$ are notable examples of brownmillerites studied for their significant ionic

conductivity.^{3,5-8} Apart from brownmillerites, there are other structures that also share the same chemical formula $A_2B_2O_5$ but have different oxygen vacancy patterns.⁴ For example, the structure of $Sr_2Mn_2O_5$ is based on corner-sharing MnO_5 square pyramids, where oxygen vacancies form a pseudo-hexagonal tunnel running along the $[001]$ direction, as illustrated in Figure 1b.⁹⁻¹¹

Fluorination presents another route for tuning the anion composition and altering physical properties. A variety of synthetic approaches to stabilize perovskite oxyfluorides have been demonstrated,¹² with much recent work focused on the use of toptactic routes in which a fluoropolymer is decomposed to provide a F vapor source to a nearby oxide sample.¹³ This toptactic fluorination reaction has been demonstrated on both bulk and epitaxial thin films samples,¹⁴⁻¹⁶ and on compounds with a wide range of B -site chemistries.¹⁷⁻²¹ Studies on the physical properties of $AB(O,F)_{3-\delta}$ oxyfluorides have generally revealed an increase in electrical resistivity, slight blue-shifts of band gaps and optical transitions, lattice expansions owing to the increased ionicity of the metal-ligand bonds, and predictions of multiferroic behavior.^{16,22-24} However, to date, this work has largely focused on perovskites with a single B -site cation, and thus the impact of fluorination on perovskites with multiple B -site cations remains unexplored.

To better understand the impact of B -site composition on F incorporation and the resultant physical properties, we have deposited a series of $SrFe_xMn_{1-x}O_{2.5}$ films and then subjected them to identical fluorination conditions to synthesize oxyfluorides. Previous work has established that both $SrB(O,F)_{3-\delta}$ oxyfluorides ($B = Mn, Fe$) can be synthesized as bulk samples or epitaxial films.^{14,15,25-27} Fluorination of $SrBO_{3-\delta}$ ($B = Mn, Fe$) oxides into $SrB(O,F)_{3-\delta}$ oxyfluorides occurs by F substituting for O in the manganite, reducing the Mn valence state, while F occupies both vacancy and O sites in the ferrite allowing Fe to maintain a preferred 3+ state.^{15,16,25,28} In both materials, F substitution has the effect of increasing the lattice volume as the B -F bonds are longer

than their *B*-O counterparts.^{25,29} With increasing F content, increased resistivity has been reported in $\text{SrMn}(\text{O},\text{F})_{3-\delta}$,²³ and a bandgap expansion has been shown via a blue-shift in optical absorption in both $\text{SrMn}(\text{O},\text{F})_{3-\delta}$ and $\text{SrFe}(\text{O},\text{F})_{3-\delta}$.^{23,24} However, fluorination of $\text{SrFe}_x\text{Mn}_{1-x}\text{O}_{2.5}$ alloys has not been reported and thus it is unknown how F incorporation and physical properties are affected by *x* in this family of complex oxyfluorides. For comparison, we also characterize the $\text{SrFe}_x\text{Mn}_{1-x}\text{O}_{2.5}$ and $\text{SrFe}_x\text{Mn}_{1-x}\text{O}_3$ oxide counterparts. While the bulk structures of $\text{Sr}_2\text{Mn}_2\text{O}_5$ and $\text{Sr}_2\text{Fe}_2\text{O}_5$ are known, the crystal structures and physical properties within the quaternary $\text{SrFe}_x\text{Mn}_{1-x}\text{O}_{2.5}$ family has not been previously reported, to our knowledge. We have also oxidized the as-grown samples to obtain an equivalent set of $\text{SrFe}_x\text{Mn}_{1-x}\text{O}_3$ films. Both SrFeO_3 and SrMnO_3 form cubic perovskites in bulk,^{30,31} although SrMnO_3 is also commonly stabilized in a hexagonal structure with edge-sharing MnO_6 octahedra.³² The lattice volume of bulk $\text{SrFe}_x\text{Mn}_{1-x}\text{O}_3$ increases systematically with increasing *x*, while its resistivity decreases with increasing Fe substitution (*x*) until reaching the metallic state in the SrFeO_3 parent compound.³³

We find that the F concentration of these oxyfluorides increases with increasing Fe substitution, which we believe arises primarily due to the brownmillerite structure supporting more rapid ion diffusion. Using X-ray photoemission spectroscopy, we find larger peak shifts associated with the Fe-F bonds compared to the Mn-F bonds, which we attribute to inductive effects. The fluorinated $\text{SrFe}_x\text{Mn}_{1-x}\text{O}_{2.5-\delta}\text{F}_\gamma$ films show higher resistivity than as-grown $\text{SrFe}_x\text{Mn}_{1-x}\text{O}_{2.5}$. The optical absorption spectra of $\text{SrFe}_x\text{Mn}_{1-x}\text{O}_{2.5}$ and $\text{SrFe}_x\text{Mn}_{1-x}\text{O}_3$ films are similar to a linear combination of the two end members $\text{SrFeO}_{2.5}$ and SrMnO_3 . In contrast, non-linear shifting of spectral weight within the absorption data is observed for $\text{SrFe}_x\text{Mn}_{1-x}\text{O}_{2.5-\delta}\text{F}_\gamma$ with changing *x*, which suggests that the incorporation of F impacts the band structure in more complex ways in the oxide $\text{SrFe}_x\text{Mn}_{1-x}\text{O}_{3-\delta}$ counterparts. These results demonstrate the compositional flexibility now possible in

epitaxial perovskite films and illustrate how combining both cationic and anionic substitutions can be used to engineer functional properties beyond simple rule of mixtures approximations.

Experimental Methods

The epitaxial $\text{SrFe}_x\text{Mn}_{1-x}\text{O}_{2.5}$ films were deposited with oxide molecular beam epitaxy (MBE) on $(\text{LaAlO}_3)_{0.3}(\text{Sr}_2\text{TaAlO}_6)_{0.7}$ (LSAT) on (001)-oriented substrates. During growth, the substrate heater was maintained at around 600°C , while the MBE growth chamber pressure was held at 2.5×10^{-6} Torr with O_2 introduced. The films were grown by the co-deposition of Sr, Mn, and Fe with a ~ 30 sec deposition rate for each unit cell, followed by a 10 sec anneal with source shutters closed between each monolayer. The films used in this study are approximately 30 nm thick as verified by X-ray reflectivity (XRR). The relative cation compositions were determined by X-ray photoelectron spectroscopy (XPS) confirming the *B*-site stoichiometry (x) of the films.

The as-grown $\text{SrFe}_x\text{Mn}_{1-x}\text{O}_{2.5}$ films were subsequently exposed to either a post-growth fluorination or oxidation reaction. The fluorination reactions were carried out using polytetrafluoroethylene (PTFE) as a precursor for a vapor transport process in which the as-grown films were placed in an alumina boat, separated by a barrier made of aluminum foil to prevent contact with the PTFE pellets. The alumina boat was covered in aluminum foil with holes on both ends and was placed in the center of a quartz tube. The tube was heated to 200°C for 4 h under flowing Ar at a rate of approximately $0.25 \text{ L} \cdot \text{min}^{-1}$.^{16,23,25} To oxidize the as-grown $\text{ABO}_{2.5}$ films into fully oxidized ABO_3 perovskites, an oxygen plasma anneal was performed for the $\text{SrFe}_x\text{Mn}_{1-x}\text{O}_{2.5}$ films ($x = 0, 0.25, 0.5, 0.75$), and ozone anneal was performed for $\text{SrFeO}_{2.5}$ ($x = 1$). The plasma anneal was achieved by heating the as-grown film inside the MBE main chamber in oxygen plasma at 1×10^{-5} Torr.³⁴ During the plasma treatment, the sample was heated to $\sim 600^\circ\text{C}$ for 1

hour, then the temperature was gradually stepped down in increments of about 50°C and allowed to sit for 30 min at each temperature step. After the substrate heater reached zero current, the sample was held for another hour in the plasma. The ozone anneal was performed by placing the as-grown SrFeO_{2.5} film in the quartz tube in a flowing O₃/O₂ mixture gas at 150°C for 1 hour.

X-ray diffraction (XRD) and x-ray reflectivity were measured using a Rigaku SmartLab diffractometer. XRD simulations were performed using the GenX software package to extract accurate *c*-axis parameters.³⁵ XPS depth profiling using carried out using a Physical Electronics VersaProbe 5000 instrument with 1 keV Ar⁺ ions for sputtering. Electronic transport experiments were performed with silver paint contacts in a van der Pauw geometry in a Physical Properties Measurement System (Quantum Design). Optical absorption spectra were obtained using variable angle spectroscopic ellipsometry (J.A. Woolam M-200U) with data collected at five incident angles from 65–75° at room temperature.

Results

Figure 1c shows the XRD data of the as-grown SrFe_xMn_{1-x}O_{2.5}, plasma annealed SrFe_xMn_{1-x}O₃, and fluorinated SrFe_xMn_{1-x}O_{2.5-δ}F_γ films. There are 15 films plotted in 5 groups associated with different cation compositions ($x = 0, 0.25, 0.5, 0.75, 1$). The obtained *c*-axis parameters of each film are plotted in Figure 1d as a function of *x*. The *c*-axis parameter of our as-grown SrMnO_{2.5} film is 3.802 Å, which agrees with previously reported *c*-axis values for SrMnO_{2.5} on LSAT, which have ranged from 3.790 to 3.811 Å.^{25,36} Previous structural studies have shown that epitaxial SrMnO_{2.5} films on LSAT grow with the bulk orthorhombic *c*-axis of SrMnO_{2.5} parallel to the *c*-axis of the substrate, thus leading to the oxygen vacancy channels running along the out-of-plane film direction.³⁶ The *c*-axis parameter of our as-grown SrFeO_{2.5} film is 4.013 Å, which also agrees with previously reported values for SrFeO_{2.5}/LSAT.³⁷ The orientation of the oxygen

vacancy planes in the as-grown $\text{SrFeO}_{2.5}$ films is unknown. While DFT calculations indicate that ordering of the vacancies within the pseudocubic (100) and (010) planes is energetically favorable,³⁸ recent experimental work has demonstrated that both horizontal and vertical vacancy ordering can be stabilized in $\text{SrFeO}_{2.5}$ /LSAT depending on the synthesis conditions.³⁹ For the as-grown $\text{SrFe}_x\text{Mn}_{1-x}\text{O}_{2.5}$ films, we observed a c -axis expansion from $\text{SrMnO}_{2.5}$ to $\text{SrFeO}_{2.5}$ with increasing x (Figure 1d). The exact crystal structure of the as-grown alloyed films ($x = 0.25, 0.5, 0.75$) is unknown, but are hypothesized to lack long-range order of the oxygen vacancies due to the disordered distribution of Fe and Mn on the B -site positions. In a previous report of bulk $\text{Sr}_2\text{FeMnO}_{5+y}$, the O vacancies were found to be disordered but the (Fe,Mn)-O bond lengths were very close to the average of Fe-O and Mn-O bond lengths in $\text{Sr}_2\text{Fe}_2\text{O}_5$ and $\text{Sr}_2\text{Mn}_2\text{O}_5$, respectively.⁴⁰ The lattice constant of bulk $\text{Sr}_2\text{Mn}_2\text{O}_5$ is ~ 3.84 Å,⁴¹ smaller than that of $\text{Sr}_2\text{Fe}_2\text{O}_5$ ~ 4.00 Å.^{5,6} Therefore, the lattice expansion with increasing Fe substitution (x) is to be expected based on the bulk structures.

After oxidation, the nominal 3+ state of Mn in $\text{SrMnO}_{2.5}$ is increased to 4+ in SrMnO_3 . Our observation of a decreased c -axis parameter of SrMnO_3 compared to $\text{SrMnO}_{2.5}$ is consistent with the lattice contraction that has been observed in manganites upon decreasing the oxygen vacancy concentration.⁴² After oxidation, the Fe^{3+} is oxidized to the nominal Fe^{4+} state with a smaller ionic size resulting in a decreased c -axis parameter.^{14,43} For the mixed B -site $\text{SrFe}_x\text{Mn}_{1-x}\text{O}_3$ films ($0 < x < 1$), the lattice parameter increases with x due to the substitution of larger Fe^{4+} ions for the smaller Mn^{4+} ions.⁴⁴ The slope of the c -axis parameter of $\text{SrFe}_x\text{Mn}_{1-x}\text{O}_3$ as a function of x becomes smaller when $x > 0.5$, which is consistent with the decreased slope of lattice parameter with increasing x observed in bulk $\text{SrFe}_x\text{Mn}_{1-x}\text{O}_3$ when $x > 0.5$.³³ The non-linear expansion of c with x is attributed to the stronger hybridization of Fe $3d$ -O $2p$ compared to Mn $3d$ -O $2p$, which makes the Fe-O bond

more covalent than Mn-O.⁴⁵ This is consistent with previous work illustrating that increased covalency of the *B*-O bond results in a smaller lattice size.⁴⁶

Contrary to oxidation, the *c*-axis parameter expands after fluorination for each film. This F-induced lattice expansion is consistent with numerous previous studies showing an expansion of lattice volume in oxyfluorides compared to perovskite oxides.^{15,16,23,25,28,47,48} The lattice expansion of fluorinated SrBO_{2.5-δ}F_γ is interpreted by the F⁻/O²⁻ substitution-induced reduction of Fe/Mn ions and consequently longer bond distance of *B*-(O,F) due to increased ionicity.¹⁶ As shown in Figure 1d, the relative *c*-axis expansion value increases with the increasing Fe substitution (*x*). According to previous studies, the degree of *c*-axis expansion positively correlates with F content (*γ*) for both SrFeO_{2.5-δ}F_γ and SrMnO_{2.5-δ}F_γ.^{16,23}

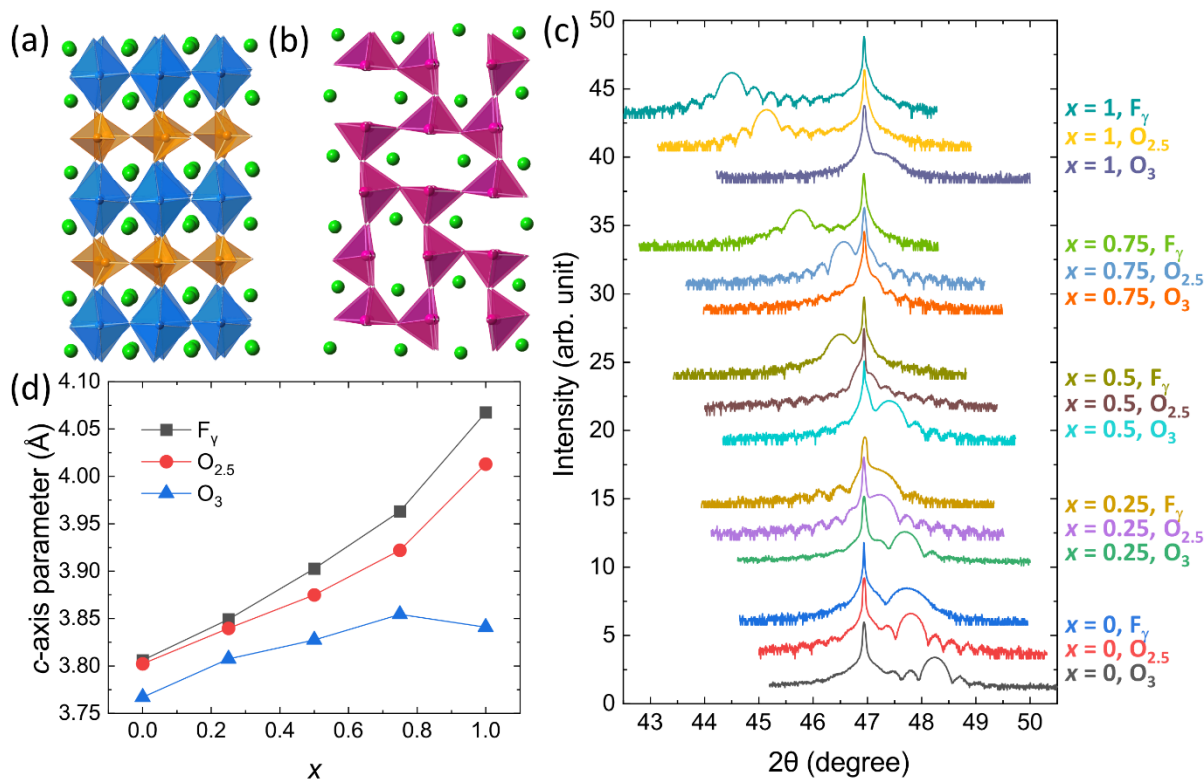


Figure 1. Crystal structures of bulk (a) Sr₂Fe₂O₅ and (b) Sr₂Mn₂O₅. (c) XRD data of as-grown SrFe_xMn_{1-x}O_{2.5}, fluorinated SrFe_xMn_{1-x}O_{2.5-δ}F_γ, and oxidized SrFe_xMn_{1-x}O₃ films showing the pseudocubic 002 reflection. The sharp peak near 47° is the LSAT 002. (d) The *c*-axis parameters as a function of *x* for the three different anionic compositions.

The F content of each SrFe_xMn_{1-x}O_{2.5-δ}F_γ film was probed by XPS. Figure 2 shows the F content (γ) as a function of *x*, and the 2*p* photoelectron spectra of Mn and Fe in the fluorinated films. Each film was fluorinated at the same condition, 200°C for 4 h with PTFE as the fluorine source. The F content is obtained by averaging the XPS depth profile through the film, which is shown in Figure S1. The atomic concentration of each element is normalized by the atomic percent of Sr, as listed in Table S1. As shown in Figure 2a, the fluorinated *x* = 0 film has the lowest F content. The F concentration increases continually as more Fe is substituted for Mn; the *x* = 1 film

has the highest F content. We attribute the trend in F incorporation to an increase in the F diffusion coefficient in SrFeO_{2.5} compared to SrMnO_{2.5}, which is consistent with the commonly reported large ionic conductivity in brownmillerite Sr₂Fe₂O₅.^{7,49} In contrast, Sr₂Mn₂O₅ does not appear to exhibit ionic conductivity comparable to Sr₂Fe₂O₅.⁵⁰ The $x = 0$ and 0.25 oxyfluorides also have a significant decrease in the measured F concentration from the initial spectra (top surface layer before sputtering) to the spectra obtained after the first sputtering cycle (near-sub-surface region). This suggests that the incorporation process associated with F movement from the surface to within the crystal lattice is also a rate limiting step, especially in the Mn-rich samples. The increased F content with increasing x is also consistent with the increased c -axis expansion of SrFe _{x} Mn_{1- x} O_{2.5- δ} F _{γ} with increasing x , shown in Figure 1d. We note that we do not have a direct measurement of δ within the films. However, the reduction of Mn in SrMnO_{2.5- δ} F _{γ} films indicates that $\delta < \gamma < 2\delta$, as $\gamma = \delta$ will induce a reduction from 3+ to 2.5+ while the limit of $\gamma = 2\delta$ would not alter the average B -site oxidation state.

Further information on the Mn and Fe bonding comes from the $2p$ photoelectron spectra. Figure 2b shows the Mn $2p$ photoelectron spectra of fluorinated films and as-grown SrMnO_{2.5}. For the as-grown SrMnO_{2.5}, the Mn $2p_{3/2}$ peak is located at 640.6 eV; after fluorination, the Mn $2p_{3/2}$ peak of SrMnO_{2.5- δ} F _{γ} ($x = 0$) shifts to 642.1 eV. This is consistent with the formation of Mn-F bonds after fluorination.²⁵ As reported in bulk materials, the Mn $2p_{3/2}$ peak is located at lower binding energy in Mn oxides (641.5 eV for MnO and Mn₂O₃) than in Mn fluorides (642.8 eV for MnF₂ and MnF₃).⁵¹ However, for each of the alloyed ($x = 0.25, 0.5, 0.75$) oxyfluoride films, the Mn $2p_{3/2}$ peak shifts back to the position of Mn $2p_{3/2}$ peak in as-grown SrMnO_{2.5}, despite the increased F content (γ) observed with Fe substitution (Figure 2a).

The Fe $2p$ photoelectron spectra are shown in Figure 2c. The Fe $2p_{3/2}$ peaks of all $\text{SrFe}_x\text{Mn}_{1-x}\text{O}_{2.5-\delta}\text{F}_\gamma$ ($x = 0.25, 0.5, 0.75, 1$) oxyfluoride films are located at the same position around 710 eV with minimal spectral change as x is increased from 0.25 to 1, where the Fe $2p_{3/2}$ peak of as-grown $\text{SrFeO}_{2.5}$ resides at around 709.5 eV. The Fe $2p_{3/2}$ peak of Fe oxides is located at lower binding energy than Fe fluorides in bulk.⁵² Therefore, the Fe $2p_{3/2}$ peak positions within the $\text{SrFe}_x\text{Mn}_{1-x}\text{O}_{2.5-\delta}\text{F}_\gamma$ films with $x = 0.25, 0.5, 0.75,$ and 1 indicate the formation of Fe-F bonds. The satellite peaks of Fe $2p$ are sensitive to the oxidization state and the ligand electronegativity. After fluorination, a satellite peak is visible at around 720 eV in the $\text{SrFeO}_{2.5-\delta}\text{F}_\gamma$ films ($x = 1$). In the $x = 0.75, 0.5,$ and 0.25 samples, the satellite peak of the fluorinated $\text{SrFe}_x\text{Mn}_{1-x}\text{O}_{2.5-\delta}\text{F}_\gamma$ films is located at around 717 eV. The satellite peak shifting to lower binding energy is consistent with the reduction of Fe.^{16,53} Therefore, the addition of Mn to the B -sites appears to promote the reduction of some Fe^{3+} cations to Fe^{2+} . Additionally, in the $x = 1$ $\text{SrFeO}_{2.5}$ and $\text{SrFeO}_{2.5-\delta}\text{F}_\gamma$ films, a shoulder feature was observed near 707 eV, which is attributed to sputter-induced formation of reduced Fe, such as in FeO species,⁵⁴ as this feature is not present on the film surface and increases in intensity with increasing sputter cycles as shown in Figure S2.

In the B -site alloyed oxyfluoride films, the F incorporation will form Fe-F-Fe, Mn-F-Mn, and Fe-F-Mn bonds. Because the electronegativity of Mn is smaller than Fe, F tends to share its electrons more prominently with Fe due to the inductive effect, in which the covalency of a metal-ligand bond is influenced by the presence of additional metals or anions in the crystal with differing degrees of electronegativity.^{55,56} Therefore, the photoemission signature of Fe-F bonds is more pronounced than for the Mn-F bonds. However, because the Fe $2p_{3/2}$ peak shifting of $\text{SrFeO}_{2.5-\delta}\text{F}_\gamma$ ($x = 1$) compared with as-grown $\text{SrFeO}_{2.5}$ is small (~ 0.5 eV), we are unable to determine if the Fe $2p_{3/2}$ peak shifts to higher binding energy with increasing amounts of F.

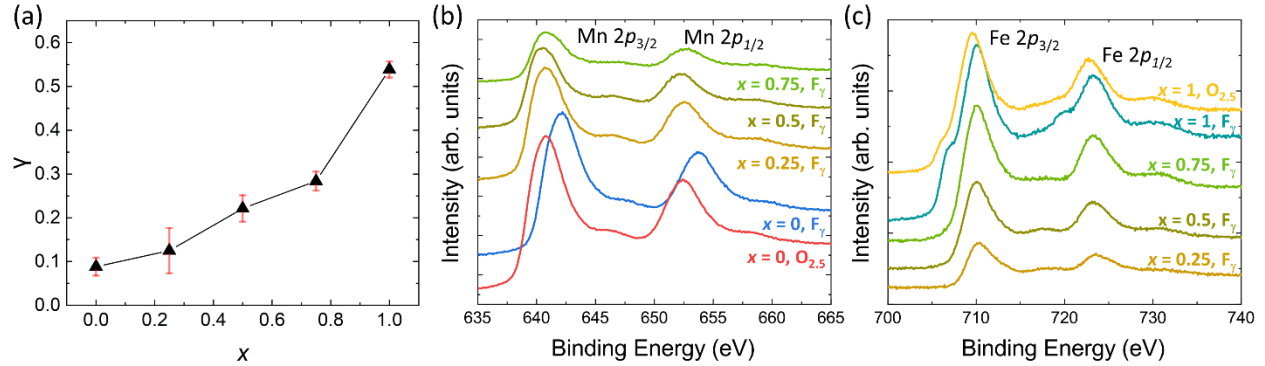


Figure 2. (a) The F content, γ , as a function of Fe composition, x . These data were measured from the fluorinated samples in Figure 1. The (b) Mn 2p and (c) Fe 2p photoelectron spectra of different $SrFe_xMn_{1-x}O_{2.5-\delta}F_\gamma$ films, along with the Mn 2p and Fe 2p of as-grown $SrMnO_{2.5}$ and $SrFeO_{2.5}$ films as references.

Temperature-dependent electronic resistivity data are shown in Figure 3; all samples are insulators except $SrFeO_3$. $SrFeO_{2.5}$, $SrFe_{0.75}Mn_{0.25}O_{2.5-\delta}F_\gamma$, and $SrFeO_{2.5-\delta}F_\gamma$ are too resistive for our measurement capabilities ($\rho > 10^4 \Omega \cdot \text{cm}$) even at 380 K. For the as-grown $SrFe_xMn_{1-x}O_{2.5}$ films shown in Figure 3a, increasing the Fe content results in a larger resistivity, which increases exponentially with decreasing temperature. The resistivity at 300 K are plotted in Figure S3b to enable comparisons between different anion compositions as a function of x . After fluorination, as shown in Figure 3c, resistivity increases for all values of x , consistent with our previous study of $SrMnO_{2.5-\delta}F_\gamma$.²³ Both $SrFeO_{2.5}$ and $SrFeO_{2.5-\delta}F_\gamma$ were too resistive to measure, so the impact of fluorination on transport in the $x = 1$ material is unclear. After oxidation, all films became more conductive with the largest effect for the $SrFeO_3$ film, which shows metallic behavior. The $SrFeO_3$ resistivity is about $1.9 \text{ m}\Omega \cdot \text{cm}$ at room temperature and exhibits a $\rho_{300\text{K}}/\rho_{10\text{K}}$ ratio of 25.8. A slight hysteresis, observed at $\sim 100 \text{ K}$, is consistent with transport reported in bulk $SrFeO_3$.^{37,57} Oxidized

SrMnO₃ has a lower resistivity than SrMnO_{2.5}, but is still an insulator, consistent with previous literature.^{23,58} Other SrFe_xMn_{1-x}O₃ films are all insulators but with lower resistivity compared with the as-grown films. The resistivity increases with x , reaches a maximum when $x = 0.5$ and decreases with further Fe substitution as shown in Figure 3b. A similar non-monotonic trend was found in bulk SrFe_xMn_{1-x}O₃ where resistivity reaches the maximum when $x = 0.1$.³³ Previous studies of the SrFe_xMn_{1-x}O₃ electronic structure showed that the Fe 3*d* bandwidth is larger than that of Mn 3*d*, which was attributed to the stronger hybridization of Fe 3*d*-O 2*p* compared to Mn 3*d*-O 2*p*.⁴⁵ The higher covalency of Fe-O bonds leads to a metallic behavior of SrFeO₃, also consistent with the reduced slope of *c*-axis parameter expansion with increased x when $x > 0.5$ shown in Figure 1d.

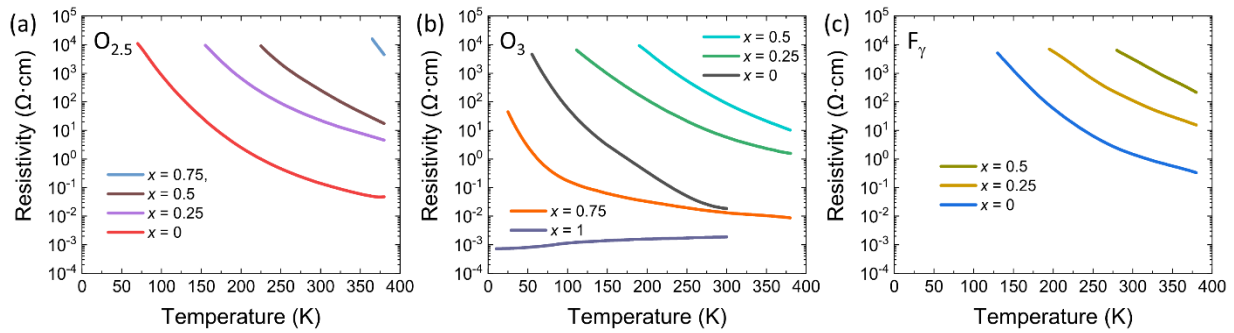


Figure 3. Resistivity as a function of temperature in (a) SrFe_xMn_{1-x}O_{2.5}, (b) SrFe_xMn_{1-x}O₃, and (c) fluorinated SrFe_xMn_{1-x}O_{2.5- δ} F _{γ} films.

We fit the resistivity using a basic Arrhenius equation to determine activation energies for electronic conductivity (Figure S3a). The obtained activation energy of each film, along with the 300 K resistivity, are displayed inset of Figure S3b. Similar to the resistivity data, for the as-grown SrFe_xMn_{1-x}O_{2.5} and fluorinated SrFe_xMn_{1-x}O_{2.5- δ} F _{γ} films, the activation energies increase with increasing x and after fluorination. The obtained activation energy of 130 meV for SrMnO₃ is

consistent with previously reported 160 meV for SrMnO₃ epitaxial films on LSAT.⁵⁹ However, for the oxidized SrFe_xMn_{1-x}O₃ films, the resistivity increases (up to $x = 0.5$) and then decreases with further Fe substitution (x from 0.5 to 1). The activation energy shown in the inset of Figure S3b doesn't show a clear trend of the oxidized SrFe_xMn_{1-x}O₃ films, but the $x = 0.5$ film exhibits the highest activation which is consistent with the highest resistivity at 300 K when $x = 0.5$.

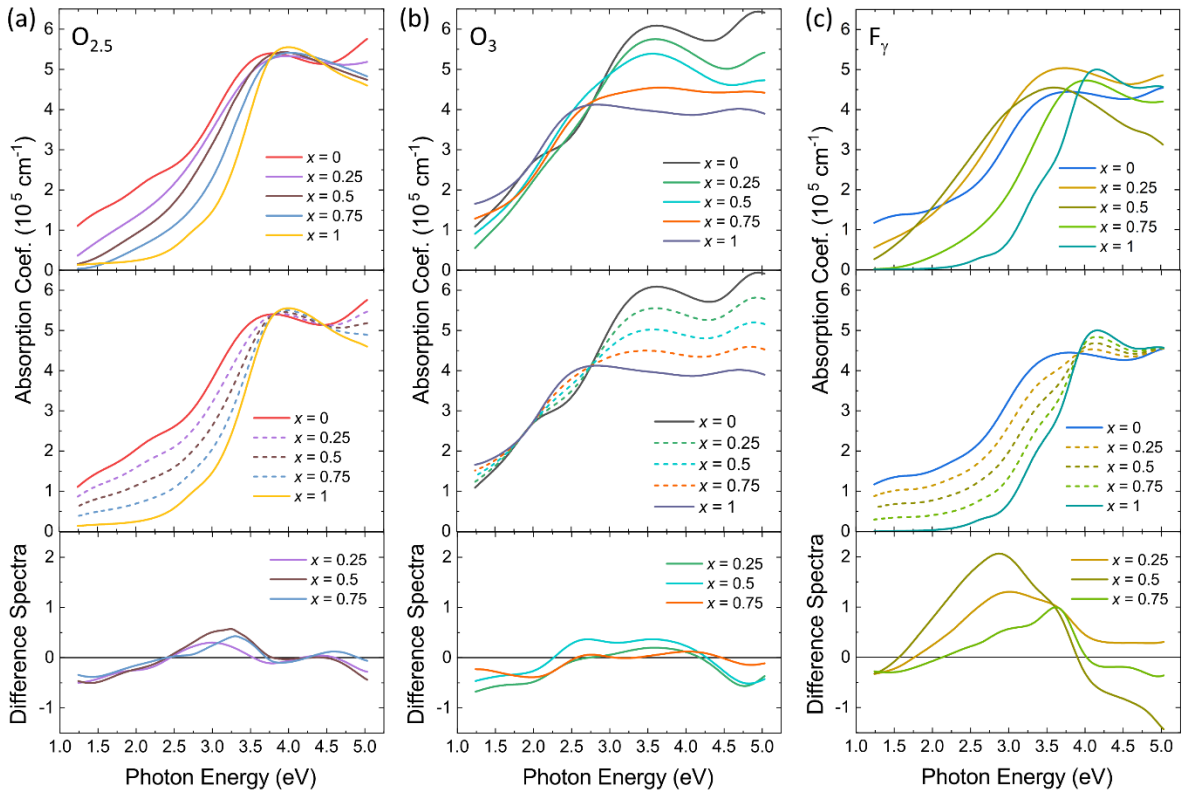


Figure 4. The optical absorption spectra (top), the simulated absorption spectra for the mixed B -site alloys (dashed lines in middle panels), and the difference between the measured and simulated spectra (bottom) of (a) as-grown SrFe_xMn_{1-x}O_{2.5}, (b) oxidized SrFe_xMn_{1-x}O₃, and (c) fluorinated SrFe_xMn_{1-x}O_{2.5-δ}F_γ films.

The absorption coefficients as a function of photon energy were obtained using spectroscopic ellipsometry. Figure 4 shows the optical absorption spectra for as-grown $\text{SrFe}_x\text{Mn}_{1-x}\text{O}_{2.5}$, oxidized $\text{SrFe}_x\text{Mn}_{1-x}\text{O}_3$, and fluorinated $\text{SrFe}_x\text{Mn}_{1-x}\text{O}_{2.5-\delta}\text{F}_\gamma$ films. Alternatively, the absorption data are plotted in five groups with $x = 0, 0.25, 0.5, 0.75,$ and 1 in Figure S4 to show the impact of anionic composition at fixed cation stoichiometry. For as-grown $\text{SrFe}_x\text{Mn}_{1-x}\text{O}_{2.5}$ films (top panel of Figure 4a), a clear trend is present from $\text{SrMnO}_{2.5}$ to $\text{SrFeO}_{2.5}$, as the absorption edge shifts to higher photon energy (blue-shift) with increasing Fe substitution. This trend could possibly be attributed to two factors: first, the Fe substitution increases the overall transition energy between O $2p$ and Mn/Fe $3d$ states, the energy of which evolve with x , leading to a blue-shift. Second, the incorporation of Fe simply leads to a new Fe $3d$ band, such that intermediate $\text{SrFe}_x\text{Mn}_{1-x}\text{O}_{2.5}$ compounds ($0 < x < 1$) act as a linear combination of the $\text{SrFeO}_{2.5}$ and $\text{SrMnO}_{2.5}$ films. To test these two scenarios, we simulated the absorption spectra of $\text{SrFe}_x\text{Mn}_{1-x}\text{O}_{2.5}$ films ($x = 0.25, 0.5,$ and 0.75) using the measured $\text{SrFeO}_{2.5}$ and $\text{SrMnO}_{2.5}$ absorption. The simulated absorption (α_{sim}) of $\text{SrFe}_x\text{Mn}_{1-x}\text{O}_{2.5}$ is calculated as $\alpha_{sim} = x\alpha_{SFO} + (1 - x)\alpha_{SMO}$ and is plotted in the middle panel of Figure 4a. The difference spectra, defined by subtracting the simulated spectra from the measured data, are plotted in the bottom panel of Figure 4a. The simulated spectra show the same basic spectral shape as that measured from the $\text{SrFe}_x\text{Mn}_{1-x}\text{O}_{2.5}$ films ($x = 0.25, 0.5,$ and 0.75). The difference between the simulation and the experimental data is within 10%.

After oxidation, the absorption edge of all $\text{SrFe}_x\text{Mn}_{1-x}\text{O}_3$ films shift to lower photon energy (red-shift) compared with the as-grown $\text{SrFe}_x\text{Mn}_{1-x}\text{O}_{2.5}$ films, as shown in Figure S4. For the both end members $\text{SrMnO}_{2.5}$ ($x = 0$) and $\text{SrFeO}_{2.5}$ ($x = 1$), the red-shift after oxidation has been attributed in previous studies to a broadening of the O $2p$ bandwidth for SrMnO_3 (SrFeO_3) compared to $\text{SrMnO}_{2.5}$ ($\text{SrFeO}_{2.5}$) and the emergence of new empty states above the Fermi level.^{23,60,61} The

simulated and difference spectra are also plotted in the middle and bottom panels, respectively, in Figure 4b. A similar trend of the absorption spectra with increasing x is observed in simulated spectra. Therefore, the absorption of the oxide $\text{SrFe}_x\text{Mn}_{1-x}\text{O}_3$ and $\text{SrFe}_x\text{Mn}_{1-x}\text{O}_{2.5}$ films can be approximated by a linear combination of parent ternary compounds.

For the fluorinated $\text{SrFe}_x\text{Mn}_{1-x}\text{O}_{2.5-\delta}\text{F}_\gamma$ films, the absorption coefficients could be influenced by the Fe substitution, F content, and the O vacancies. The measured and simulated absorption spectra of $\text{SrFe}_x\text{Mn}_{1-x}\text{O}_{2.5-\delta}\text{F}_\gamma$ films along with the difference spectra are plotted in the top, middle, and bottom panels respectively in Figure 4c. Comparing the measured and simulated spectra, the optical absorption of $\text{SrFe}_x\text{Mn}_{1-x}\text{O}_{2.5-\delta}\text{F}_\gamma$ does not follow a linear combination of $\text{SrMnO}_{2.5-\delta}\text{F}_\gamma$ and $\text{SrFeO}_{2.5-\delta}\text{F}_\gamma$. One possible factor is the difference in F content for each film, as shown in Figure 2a, which does not follow an exact linear dependence on x . Another likely origin of this phenomena is the influence of the countercation Mn on the Fe-F bonds (and vice versa) as revealed by the photoemission spectra. In the bottom panel of Figure 4c, there is a trend of the peak within the difference spectra shifting to higher photon energy with increasing x . Since the highest intensity peak position of $\text{SrFeO}_{2.5-\delta}\text{F}_\gamma$ is in higher photon energy than $\text{SrMnO}_{2.5-\delta}\text{F}_\gamma$, the difference peak shifting presumably indicates the Fe $3d$ and F $2p$ interaction is enhanced. These results suggest that the combination of cationic and anionic substitutions, in which the covalency of the metal-ligand bond is influenced by the presence of a second B -site cationic and anionic element, can result in non-trivial changes to band structure, making this a fertile strategy for design and discovery of materials with novel electronic, optical or magnetic function.

Conclusion

We synthesized a series of $\text{SrFe}_x\text{Mn}_{1-x}\text{O}_{2.5}$ epitaxial films with five different cation compositions and converted these films into $\text{SrFe}_x\text{Mn}_{1-x}\text{O}_{2.5-\delta}\text{F}_\gamma$ oxyfluorides by a topotactic

fluorination method; we also oxidized the as-grown films into $\text{SrFe}_x\text{Mn}_{1-x}\text{O}_3$ perovskites. The F content increases with the increasing Fe substitution and reaches the maximum at $x = 1$. The photoelectron spectra of Mn and Fe $2p$ indicates the F anions have a more significant impact on the Fe bonding state than the Mn. The electronic transport measurements show that fluorination increases the resistivity for all films. The optical absorption of the $0 < x < 1$ oxide films are well-described by a linear combination of the parent compounds $\text{SrMnO}_{2.5}$ (SrMnO_3) and $\text{SrFeO}_{2.5}$ (SrFeO_3), which indicates the Fe substitution introduces a Fe $3d$ state into the electronic structure without significantly modifying the Mn-derived bands. For the fluorinated $\text{SrFe}_x\text{Mn}_{1-x}\text{O}_{2.5-\delta}\text{F}_\gamma$ films, the F incorporation induces non-linear changes to band structure, with the spectral difference peak shifting towards $\text{SrFeO}_{2.5-\delta}\text{F}_\gamma$, which is consistent with an enhanced Fe-F interaction as revealed by XPS. This work demonstrates that the combination of *B*-site cation and F anion substitution results in non-trivial changes to the structural, electronic and optical properties, enabling new paths to engineer the properties in functional heteroanionic materials.

Supporting Information

The supporting information is available free of charge at [<https://pubs.acs.org/...>].

XPS depth profiles of $\text{SrFe}_x\text{Mn}_{1-x}\text{O}_{2.5-\delta}\text{F}_\gamma$ films; Arrhenius fitting of the resistivity data; optical absorption spectra of as-grown $\text{SrFe}_x\text{Mn}_{1-x}\text{O}_{2.5}$, fluorinated $\text{SrFe}_x\text{Mn}_{1-x}\text{O}_{2.5-\delta}\text{F}_\gamma$, and plasma annealed $\text{SrFe}_x\text{Mn}_{1-x}\text{O}_3$ films plotted at constant cation compositions to highlight the effects of anionic composition.

Notes

The authors declare no competing financial interests.

* smay@drexel.edu

Acknowledgements

This work was supported by the National Science Foundation (CMMI-1562223). We acknowledge use of the Materials Characterization Core facilities at Drexel.

References

- (1) Kageyama, H.; Hayashi, K.; Maeda, K.; Attfield, J. P.; Hiroi, Z.; Rondinelli, J. M.; Poeppelmeier, K. R. Expanding frontiers in materials chemistry and physics with multiple anions. *Nat. Commun.* **2018**, *9*, 772.
- (2) Herklotz, A.; Lee, D.; Guo, E.-J.; Meyer, T. L.; Petrie, J. R.; Lee, H. N. Strain coupling of oxygen non-stoichiometry in perovskite thin films. *J. Phys. Condens. Matter* **2017**, *29*, 493001.
- (3) Goodenough, J. B.; Ruiz-Diaz, J.; Zhen, Y. Oxide-ion conduction in $\text{Ba}_2\text{In}_2\text{O}_5$ and $\text{Ba}_3\text{In}_2\text{MO}_8$ ($M = \text{Ce}, \text{Hf}, \text{or Zr}$). *Solid State Ion.* **1990**, *44*, 21-31.
- (4) Anderson, M. T.; Vaughey, J. T.; Poeppelmeier, K. R. Structural similarities among oxygen-deficient perovskites. *Chem. Mater.* **1993**, *5*, 151-165.
- (5) D'Hondt, H.; Abakumov, A. M.; Hadermann, J.; Kalyuzhnaya, A. S.; Rozova, M. G.; Antipov, E. V.; Van Tendeloo, G. Tetrahedral chain order in the $\text{Sr}_2\text{Fe}_2\text{O}_5$ brownmillerite. *Chem. Mater.* **2008**, *20*, 7188-7194.
- (6) Schmidt, M.; Campbell, S. Crystal and magnetic structures of $\text{Sr}_2\text{Fe}_2\text{O}_5$ at elevated temperature. *J. Solid State Chem.* **2001**, *156*, 292-304.
- (7) Paulus, W.; Schober, H.; Eibl, S.; Johnson, M.; Berthier, T.; Hernandez, O.; Ceretti, M.; Plazanet, M.; Conder, K.; Lamberti, C. Lattice dynamics to trigger low temperature oxygen mobility in solid oxide ion conductors. *J. Am. Chem. Soc.* **2008**, *130*, 16080-16085.

- (8) Le Toquin, R.; Paulus, W.; Cousson, A.; Prestipino, C.; Lamberti, C. Time-resolved in situ studies of oxygen intercalation into SrCoO_{2.5}, performed by neutron diffraction and X-ray absorption spectroscopy. *J. Am. Chem. Soc.* **2006**, *128*, 13161-13174.
- (9) Mori, T.; Inoue, K.; Kamegashira, N.; Yamaguchi, Y.; Ohoyama, K. Neutron diffraction study of Sr₂Mn₂O₅. *J. Alloys Compd.* **2000**, *296*, 92-97.
- (10) Suescun, L.; Chmaissem, O.; Mais, J.; Dabrowski, B.; Jorgensen, J. D. Crystal structures, charge and oxygen-vacancy ordering in oxygen deficient perovskites SrMnO_x ($x < 2.7$). *J. Solid State Chem.* **2007**, *180*, 1698-1707.
- (11) Caignaert, V.; Nguyen, N.; Hervieu, M.; Raveau, B. Sr₂Mn₂O₅, an oxygen-defect perovskite with Mn (III) in square pyramidal coordination. *Mater. Res. Bull.* **1985**, *20*, 479-484.
- (12) McCabe, E. E.; Greaves, C. Fluorine insertion reactions into pre-formed metal oxides. *J. Fluor. Chem.* **2007**, *128*, 448-458.
- (13) Slater, P. Poly (vinylidene fluoride) as a reagent for the synthesis of K₂NiF₄-related inorganic oxide fluorides. *J. Fluor. Chem.* **2002**, *117*, 43-45.
- (14) Moon, E. J.; Xie, Y.; Laird, E. D.; Keavney, D. J.; Li, C. Y.; May, S. J. Fluorination of epitaxial oxides: synthesis of perovskite oxyfluoride thin films. *J. Am. Chem. Soc.* **2014**, *136*, 2224-2227.
- (15) Berry, F. J.; Ren, X.; Heap, R.; Slater, P.; Thomas, M. F. Fluorination of perovskite-related SrFeO_{3-δ}. *Solid State Commun.* **2005**, *134*, 621-624.
- (16) Katayama, T.; Chikamatsu, A.; Hirose, Y.; Takagi, R.; Kamisaka, H.; Fukumura, T.; Hasegawa, T. Topotactic fluorination of strontium iron oxide thin films using polyvinylidene fluoride. *J. Mater. Chem. C* **2014**, *2*, 5350-5356.

- (17) Clemens, O.; Kuhn, M.; Haberkorn, R. Synthesis and characterization of the $\text{La}_{1-x}\text{Sr}_x\text{FeO}_{3-\delta}$ system and the fluorinated phases $\text{La}_{1-x}\text{Sr}_x\text{FeO}_{3-x}\text{F}_x$. *J. Solid State Chem.* **2011**, *184*, 2870-2876.
- (18) Chikamatsu, A.; Maruyama, T.; Katayama, T.; Su, Y.; Tsujimoto, Y.; Yamaura, K.; Kitamura, M.; Horiba, K.; Kumigashira, H.; Hasegawa, T. Electronic properties of perovskite strontium chromium oxyfluoride epitaxial thin films fabricated via low-temperature topotactic reaction. *Phys. Rev. Mater.* **2020**, *4*, 025004.
- (19) Kobayashi, Y.; Tian, M.; Eguchi, M.; Mallouk, T. E. Ion-exchangeable, electronically conducting layered perovskite oxyfluorides. *J. Am. Chem. Soc.* **2009**, *131*, 9849-9855.
- (20) Onozuka, T.; Chikamatsu, A.; Katayama, T.; Hirose, Y.; Harayama, I.; Sekiba, D.; Ikenaga, E.; Minohara, M.; Kumigashira, H.; Hasegawa, T. Reversible changes in resistance of perovskite nickelate NdNiO_3 thin films induced by fluorine substitution. *ACS Appl. Mater. Interfaces* **2017**, *9*, 10882-10887.
- (21) Wissel, K.; Vogel, T.; Dasgupta, S.; Fortes, A. D.; Slater, P. R.; Clemens, O. Topochemical fluorination of $n = 2$ ruddlesden–popper type $\text{Sr}_3\text{Ti}_2\text{O}_7$ to $\text{Sr}_3\text{Ti}_2\text{O}_5\text{F}_4$ and its reductive defluorination. *Inorg. Chem.* **2020**, *59*, 1153-1163.
- (22) Hartman, S. T.; Cho, S. B.; Mishra, R. Multiferroism in iron-based oxyfluoride perovskites. *Inorg. Chem.* **2018**, *57*, 10616-10624.
- (23) Wang, J.; Shin, Y.; Gauquelin, N.; Yang, Y.; Lee, C.; Jannis, D.; Verbeeck, J.; Rondinelli, J. M.; May, S. J. Physical properties of epitaxial $\text{SrMnO}_{2.5-\delta}\text{F}_\gamma$ oxyfluoride films. *J. Phys. Condens. Matter* **2019**, *31*, 365602.
- (24) Katayama, T.; Chikamatsu, A.; Kamisaka, H.; Kumigashira, H.; Hasegawa, T. Experimental and theoretical investigation of electronic structure of $\text{SrFeO}_{3-x}\text{F}_x$ epitaxial thin films prepared via topotactic reaction. *Appl. Phys. Express* **2016**, *9*, 025801.

- (25) Wang, J.; Shin, Y.; Arenholz, E.; Lefler, B. M.; Rondinelli, J. M.; May, S. J. Effect of fluoropolymer composition on topochemical synthesis of $\text{SrMnO}_{3-\delta}\text{F}_\gamma$ oxyfluoride films. *Phys. Rev. Mater.* **2018**, *2*, 073407.
- (26) Lobanov, M. V.; Abakumov, A. M.; Sidorova, A. V.; Rozova, M. G.; D'yachenko, O. G.; Antipov, E. V.; Hadermann, J.; Van Tendeloo, G. Synthesis and investigation of novel Mn-based oxyfluoride $\text{Sr}_2\text{Mn}_2\text{O}_{5-x}\text{F}_{1+x}$. *Solid State Sci.* **2002**, *4*, 19-22.
- (27) Aich, P.; Meneghini, C.; Tortora, L.; Siruguri, V.; Kaushik, S.; Fu, D.; Ray, S. Fluorinated hexagonal 4H SrMnO_3 : a locally disordered manganite. *J. Mater. Chem C* **2019**, *7*, 3560-3568.
- (28) Berry, F.; Heap, R.; Helgason, Ö.; Moore, E.; Shim, S.; Slater, P.; Thomas, M. Magnetic order in perovskite-related SrFeO_2F . *J. Phys. Condens. Matter* **2008**, *20*, 215207.
- (29) Thompson, C. M.; Blakely, C. K.; Flacau, R.; Greedan, J. E.; Poltavets, V. V. Structural and magnetic behavior of the cubic oxyfluoride SrFeO_2F studied by neutron diffraction. *J. Solid State Chem.* **2014**, *219*, 173-178.
- (30) Ishiwata, S.; Tokunaga, M.; Kaneko, Y.; Okuyama, D.; Tokunaga, Y.; Wakimoto, S.; Kakurai, K.; Arima, T.; Taguchi, Y.; Tokura, Y. Versatile helimagnetic phases under magnetic fields in cubic perovskite SrFeO_3 . *Phys. Rev. B* **2011**, *84*, 054427.
- (31) Kobayashi, S.; Tokuda, Y.; Mizoguchi, T.; Shibata, N.; Sato, Y.; Ikuhara, Y.; Yamamoto, T. Quantitative analyses of oxidation states for cubic SrMnO_3 and orthorhombic $\text{SrMnO}_{2.5}$ with electron energy loss spectroscopy. *J. Appl. Phys.* **2010**, *108*, 124903.
- (32) Sacchetti, A.; Baldini, M.; Postorino, P.; Martin, C.; Maignan, A. Raman spectroscopy on cubic and hexagonal SrMnO_3 . *J. Raman Spectrosc.* **2006**, *37*, 591-596.

- (33) Kolesnik, S.; Dabrowski, B.; Mais, J.; Brown, D.; Feng, R.; Chmaissem, O.; Kruk, R.; Kimball, C. Magnetic phase diagram of cubic perovskites $\text{SrMn}_{1-x}\text{Fe}_x\text{O}_3$. *Phys. Rev. B* **2003**, *67*, 144402.
- (34) Rogge, P. C.; Chandrasena, R. U.; Cammarata, A.; Green, R. J.; Shafer, P.; Lefler, B. M.; Huon, A.; Arab, A.; Arenholz, E.; Lee, H. N.; Lee, T.-L.; Nemšák, S.; Rondinelli, J. M.; Gray, A. X.; May, S. J. Electronic structure of negative charge transfer CaFeO_3 across the metal-insulator transition. *Phys. Rev. Mater.* **2018**, *2*, 015002.
- (35) Björck, M.; Andersson, G. GenX: an extensible X-ray reflectivity refinement program utilizing differential evolution. *J. Appl. Crystallogr.* **2007**, *40*, 1174-1178.
- (36) Kobayashi, S.; Ikuhara, Y.; Yamamoto, T. Labyrinth-type domain structure of heteroepitaxial $\text{SrMnO}_{2.5}$ film. *Appl. Phys. Lett.* **2013**, *102*, 231911.
- (37) Yamada, H.; Kawasaki, M.; Tokura, Y. Epitaxial growth and valence control of strained perovskite SrFeO_3 films. *Appl. Phys. Lett.* **2002**, *80*, 622-624.
- (38) Young, J.; Rondinelli, J. M. Crystal structure and electronic properties of bulk and thin film brownmillerite oxides. *Phys. Rev. B* **2015**, *92*, 174111.
- (39) Saleem, M. S.; Song, C.; Gu, Y.; Chen, R.; Fayaz, M. U.; Hao, Y.; Pan, F. Orientation control of oxygen vacancy channels in brownmillerite $\text{SrFeO}_{2.5}$. *Phys. Rev. Mater.* **2020**, *4*, 014403.
- (40) Ramezanipour, F.; Greedan, J. E.; Siewenie, J.; Proffen, T.; Ryan, D. H.; Grosvenor, A. P.; Donaberger, R. L. Local and average structures and magnetic properties of $\text{Sr}_2\text{FeMnO}_{5+y}$, $y = 0.0, 0.5$. Comparisons with $\text{Ca}_2\text{FeMnO}_5$ and the effect of the *A*-site cation. *Inorg. Chem.* **2011**, *50*, 7779-7791.
- (41) Caignaert, V. $\text{Sr}_2\text{Mn}_2\text{O}_5$ magnetic structure. *J. Magn. Magn. Mater.* **1997**, *166*, 117-123.

- (42) Abdelmoula, N.; Guidara, K.; Cheikh-Rouhou, A.; Dhahri, E.; Joubert, J. Effects of the oxygen nonstoichiometry on the physical properties of $\text{La}_{0.7}\text{Sr}_{0.3}\text{MnO}_{3-\delta}\square_{\delta}$ manganites ($0 \leq \delta \leq 0.15$). *J. Solid State Chem.* **2000**, *151*, 139-144.
- (43) Clevenger Jr, T. R. Effect of Fe^{4+} in the System $\text{SrFeO}_3\text{-SrTiO}_3$. *J. Am. Ceram. Soc.* **1963**, *46*, 207-210.
- (44) Shannon, R. T.; Prewitt, C. T. Effective ionic radii in oxides and fluorides. *Acta Crystallogr. B Struct. Cryst. Cryst. Chem.* **1969**, *25*, 925-946.
- (45) Kim, D.; Lee, H.; Dabrowski, B.; Kolesnik, S.; Lee, J.; Kim, B.; Min, B.; Kang, J.-S. Photoemission spectroscopy study of metal-insulator transition in $\text{SrMn}_{1-x}\text{Fe}_x\text{O}_3$. *Phys. Rev. B* **2010**, *81*, 073101.
- (46) Cammarata, A.; Rondinelli, J. M. Covalent dependence of octahedral rotations in orthorhombic perovskite oxides. *J. Chem. Phys.* **2014**, *141*, 114704.
- (47) Sullivan, E.; Greaves, C. Fluorine insertion reactions of the brownmillerite materials $\text{Sr}_2\text{Fe}_2\text{O}_5$, $\text{Sr}_2\text{CoFeO}_5$, and $\text{Sr}_2\text{Co}_2\text{O}_5$. *Mater. Res. Bull.* **2012**, *47*, 2541-2546.
- (48) Katayama, T.; Chikamatsu, A.; Hirose, Y.; Fukumura, T.; Hasegawa, T. Topotactic reductive fluorination of strontium cobalt oxide epitaxial thin films. *J. Sol-Gel Sci. Technol.* **2015**, *73*, 527-530.
- (49) Auckett, J. E.; Studer, A. J.; Pellegrini, E.; Ollivier, J.; Johnson, M. R.; Schober, H.; Miiller, W.; Ling, C. D. Combined experimental and computational study of oxide ion conduction dynamics in $\text{Sr}_2\text{Fe}_2\text{O}_5$ brownmillerite. *Chem. Mater.* **2013**, *25*, 3080-3087.
- (50) Stølen, S.; Mohn, C. E.; Ravindran, P.; Allan, N. L. Topography of the potential energy hypersurface and criteria for fast-ion conduction in perovskite-related $A_2B_2O_5$ oxides. *J. Phys. Chem. B* **2005**, *109*, 12362-12365.

- (51) Carver, J.; Schweitzer, G.; Carlson, T. A. Use of X-Ray photoelectron spectroscopy to study bonding in Cr, Mn, Fe, and Co compounds. *J. Chem. Phys.* **1972**, *57*, 973-982.
- (52) Grosvenor, A.; Kobe, B.; Biesinger, M.; McIntyre, N. Investigation of multiplet splitting of Fe 2p XPS spectra and bonding in iron compounds. *Surf. Interface Anal.* **2004**, *36*, 1564-1574.
- (53) Yamashita, T.; Hayes, P. Analysis of XPS spectra of Fe²⁺ and Fe³⁺ ions in oxide materials. *Appl. Surf. Sci.* **2008**, *254*, 2441-2449.
- (54) Fondell, M.; Gorgoi, M.; Boman, M.; Lindblad, A. Surface modification of iron oxides by ion bombardment-comparing depth profiling by HAXPES and Ar ion sputtering. *J. Electron Spectrosc. Relat. Phenom.* **2018**, *224*, 23-26.
- (55) Harada, J. K.; Charles, N.; Poepelmeier, K. R.; Rondinelli, J. M. Heteroanionic materials by design: progress toward targeted properties. *Adv. Mater.* **2019**, *31*, 1805295.
- (56) Etourneau, J.; Portier, J.; Menil, F. The role of the inductive effect in solid state chemistry: how the chemist can use it to modify both the structural and the physical properties of the materials. *J. Alloys Compd.* **1992**, *188*, 1-7.
- (57) Nakamura, S.; Iida, S. New data on electrical properties and antiferromagnetism of highly oxidized perovskite SrFeO_x (2.5 < x < 3.0). *Jpn. J. Appl. Phys.* **1995**, *34*, L291.
- (58) Chmaissem, O.; Dabrowski, B.; Kolesnik, S.; Mais, J.; Brown, D.; Kruk, R.; Prior, P.; Pyles, B.; Jorgensen, J. Relationship between structural parameters and the Néel temperature in Sr_{1-x}Ca_xMnO₃ (0 ≤ x ≤ 1) and Sr_{1-y}Ba_yMnO₃ (y ≤ 0.2). *Phys. Rev. B* **2001**, *64*, 134412.
- (59) May, S. J.; Santos, T. S.; Bhattacharya, A. Onset of metallic behavior in strained (LaNiO₃)_n/(SrMnO₃)₂ superlattices. *Phys. Rev. B* **2009**, *79*, 115127.
- (60) Das, T.; Nicholas, J. D.; Qi, Y. Long-range charge transfer and oxygen vacancy interactions in strontium ferrite. *J. Mater. Chem. A* **2017**, *5*, 4493-4506.

(61) Galakhov, V. R.; Kurmaev, E. Z.; Kuepper, K.; Neumann, M.; McLeod, J. A.; Moewes, A.; Leonidov, I. A.; Kozhevnikov, V. L. Valence Band Structure and X-ray Spectra of Oxygen-Deficient Ferrites SrFeO_x. *J. Phys. Chem. C* **2010**, *114*, 5154-5159.